A theta rhythm in awake macaque V1 and V4 and its attentional modulation

Georgios Spyropoulos[a], **Conrado A. Bosman**[b,c], **Pascal Fries**[a,b,1]

[a]Ernst Strüngmann Institute (ESI) for Neuroscience in Cooperation with Max Planck Society, Deutschordenstraße 46, 60528 Frankfurt, Germany, [b]Donders Institute for Brain, Cognition and Behaviour, Radboud University Nijmegen, Kapittelweg 29, 6525 EN Nijmegen, Netherlands, and [c]Swammerdam Institute for Life Sciences, Center for Neuroscience, Faculty of Science, University of Amsterdam, Sciencepark 904, 1098 XH Amsterdam, Netherlands.

[1]To whom correspondence should be addressed. E-mail: pascal.fries@esi-frankfurt.de.

Abstract

Theta-rhythmic neuronal synchronization has been described in hippocampus and high-level visual areas. Recent studies suggest that theta in visual areas might originate in V1. We analyzed simultaneous electrocorticographic (ECoG) grid recordings of local field potentials from areas V1 and V4 of two macaque monkeys performing a selective visual attention task. We found a ≈4 Hz theta rhythm, which was strongest at sites showing visually induced gamma-band activity. This theta rhythm was coherent between V1 and V4, with a predominant V1-to-V4 Granger causal influence. Locally, theta phase was correlated with power in a narrow gamma-frequency band. These theta-rhythmic processes were reduced by selective attention to a visual stimulus contralateral to the recorded visual areas. This attentional effect was substantial, particularly compared to other reported effects of attention in area V1. We investigated, whether microsaccades (MSs) play a role in the generation or attentional modulation of theta. Stratification of MS rate between attention conditions, or elimination of MS-affected data epochs left the main results essentially unchanged. Thus, we find an MS-independent theta rhythm in the visually driven part of V1, which rhythmically modulates local gamma and entrains V4, and which is strongly reduced by attention.

Introduction

Neuronal activity shows rhythmic structure in several characteristic frequency bands (1). These different rhythms have often been linked to areas and/or functions, in which they predominate (2). The theta rhythm has primarily been described in high-level areas of awake mammalian brains in the context of higher cognitive functions. A particularly strong theta rhythm exists in rodent medial temporal lobe (MTL), in particular the hippocampus and entorhinal cortex (3, 4). This theta is found during exploratory behavior, and has been implicated in episodic memory (5-7). A similar theta rhythm also exists in the MTL of non-human and human primates during virtual maze navigation (8) and visual exploration (9, 10), and has been linked to episodic memory encoding (10-12) and working memory maintenance (13, 14).

Hippocampal theta is synchronized with a theta rhythm in prefrontal cortex (PFC) (15-17). Theta in PFC and strongly connected structures like the anterior cingulate cortex (ACC) and the posterior parietal cortex has been described when subjects exert executive control (18-23).

The theta rhythm in non-human primate PFC shows long-distance synchronization to a theta rhythm in area V4 (24, 25). This PFC-V4 theta-band synchronization and the V4 theta rhythm is pronounced during the delay period of a visual working memory task, that is, in the absence of visual stimulation. In inferotemporal cortex, a theta rhythm has been described that is phase-locked to stimulus onset (26).

A theta rhythm at 3-5 Hz has also been described in mid-level visual areas V4 and V5/MT during selective visual attention tasks. A study in macaque area MT reported that the power of high-frequency (30-120 Hz) LFP components is modulated by the phase of low-frequency (1-8 Hz) components, and that this modulation is reduced by attention to the visual stimulus

activating the recorded neurons (27). A study in macaque area V4 showed spike-field and spike-spike coherence at 2-4 Hz and straddling the lower end of the spectrum (28). This local low-frequency synchronization was enhanced by visual stimulation; furthermore, it was reduced by attention in the absence of visual stimulation. A subsequent study reported that the 4 Hz phase of LFP in macaque V4 modulates the gamma-band synchronization between areas V4 and V1 (29). Also theta-band Granger causality (GC) influences around 4 Hz between V1 and V4 are stronger in the feedforward direction (30). This suggests that a 4 Hz rhythm might emerge in area V1 and entrain higher areas. Interestingly, a previous study found that microsaccades occur at a 3-4 Hz rhythm and lead to evoked responses and perturbations in local synchronization in both, areas V1 and V4 (31). This MS-related V1 4 Hz rhythm temporally structures also the V1-V2 interaction by co-modulating respective gamma power and frequency (32).

Thus, several studies suggest a theta rhythm in V1, by e.g. showing a theta modulation of V1-V4 or V1-V2 interactions. Here, we analyzed simultaneous LFP recordings from awake macaque V1 and V4. We investigated whether the respective LFP power and phase-locking spectra actually show theta peaks, how this is related to visually induced activity, whether local gamma-band power is modulated by theta phase, to which degree these theta-related phenomena are independent of MSs, and whether they are modulated by selective visual attention.

Results

Macaque areas V1 and V4 show a theta rhythm. We first calculated power spectra averaged over all electrodes on V1 and V4 from periods, during which the monkey fixated and covertly monitored one of two simultaneously presented drifting grating stimuli (see Materials and Methods for the definition of “electrodes” versus “sites” and the attribution of electrodes and sites to areas). Those average power spectra exhibited clear peaks in the gamma and the beta range, with peak frequencies specific to each monkey; however, they did not exhibit clear peaks in the theta-frequency range (Fig. 1A,B). We have previously found that power spectra can fail to reveal rhythms that are nevertheless unequivocally detectable with metrics of phase locking (35, 50). Here, we quantified phase locking by means of the pairwise phase consistency metric (PPC, see Materials and Methods). We calculated PPC spectra averaged over all possible pairs of sites within and between V1 and V4. The average PPC spectra confirmed the gamma and beta peaks and in addition revealed clear theta peaks around 4 Hz (Fig. 1C,D). Thus, awake macaque visual cortex shows a distinct theta rhythm, when activated by a visual stimulus.

Selective attention reduces theta. Previous studies reported similar theta or low-frequency rhythms in awake macaque areas V4 and MT, which were reduced by selective attention (27, 51). Theta might be generated in those extrastriate areas, or it might alternatively emerge already at earlier stages of the visual system. A previous study has found that Granger-causality between visual areas in the theta band is stronger in the feedforward than feedback

direction (30). Thus, theta in extrastriate cortex might actually be driven by theta in primary visual cortex. Therefore, we investigated the theta rhythm separately in areas V1 and V4, and we tested if it was affected by selective attention. Raw power spectra averaged over all V1 electrodes showed a shallow bump around 4 Hz (Fig. 2A). This V1 theta rhythm was reduced when attention was directed to the contralateral visual stimulus, which was driving part of the V1 electrodes. A similar pattern was found in V4: There was a very shallow bump with an attentional reduction close to 4 Hz (Fig. 2B).

To reduce the $1/f^n$ component of the power spectrum, we estimated it by robust regression and subtracted it from the total power (52). We followed this approach and found that in the absence of attention, there were distinct peaks around 4 Hz in both V1 and V4 (Fig. 2C,D). Those peaks were reduced when attention was directed to the contralateral hemifield.

We also calculated low-frequency phase-locking (PPC) spectra separately for pairs of sites within V1 or V4 and between V1 and V4, and we investigated whether this phase locking is affected by selective attention. The PPC spectra showed theta peaks for pairs of sites within and between V1 and V4, and this theta-band PPC was reduced by attention (Fig. 3).

Theta is spatially coextensive with visually induced gamma. Because theta was modulated by attention, while attention was directed to visual stimuli, we next investigated whether theta was related to visually induced activity. The ECoG covered large parts of V1, corresponding to large parts of the representation of the lower right visual quadrant, from the fovea out to about six degrees of visual angle. This allowed us to test whether theta was coextensive with visually driven activity. A given ECoG electrode does not provide conventional spike recordings, yet it does provide gamma power enhancements selectively for particular stimulus positions, that is, gamma power enhancements with circumscribed receptive fields (RFs) (29, 37). The electrodes over V1 had varying overlap with the employed grating patch, which resulted in a topographic map of visually induced gamma-band power with a clear peak at the representation of the stimulus (Fig. 4A). When we calculated a corresponding topographic map of theta power (after robust regression of the $1/f^n$ component and its removal), it also showed a clear spatial peak (Fig. 4B). We calculated the spatial correlation (Spearman rank correlation) between low-frequency components (power residuals) and visually induced gamma power, across electrodes, separately for V1 and V4, for each attention condition, and for each of the low frequency components up to 10 Hz. The resulting correlation spectra reveal that across the spatial extension of both V1 and V4, visually induced gamma is positively correlated with theta when attention is ipsilateral (Fig. 4C,D, blue lines). In addition, visually induced gamma is negatively correlated with power around 1-4 Hz when attention is contralateral, and in V4 also when attention is ipsilateral (Fig. 4C,D). To ensure that the correlations shown in Figure 4C, D are not due to broadband power correlations, the analyses used gamma from the pre-cue period and theta power from the post-cue period (both with visual stimulation), that is, from non-overlapping trial epochs. Results are essentially the same if the post-cue period is used for both (data not shown).

Theta-band Granger causality is stronger in the feedforward direction and reduced by attention. The PPC analysis revealed clear theta peaks for the visually driven sites, and a previous study found theta-band GC between visual areas to be generally stronger in the feedforward direction (30). Therefore, we next investigated in detail the GC between V1 and V4 in the low-frequency range and separately for the two attention conditions. Figure 5A shows the GC spectra averaged over all V1-V4 site pairs, pooled across both attention conditions, and separately for the feedforward (V1-to-V4; green line) and feedback (V4-to-V1; black line) directions. These GC spectra reveal clear theta peaks, and they confirm that GC is stronger in the feedforward than feedback direction. To investigate whether this asymmetry in GC is due to differences in theta power between V1 and V4, we stratified theta power between the two areas. After stratification, the result remained qualitatively unchanged (data not shown).

Figure 5B shows the feedforward GC spectra separately for the two attention conditions. It reveals that feedforward GC in the theta band is enhanced when attention is to the ipsilateral stimulus. Figure 5C shows that the same pattern of attention effects exists for the feedback GC.

Theta-gamma phase-amplitude coupling and its attentional modulation. Several previous studies have found that the theta phase modulates gamma power, that is, there is theta-gamma phase-amplitude coupling, or PAC (13, 16, 19, 53). One of those studies also reported that theta-gamma PAC in area MT is decreased with attention to the activating stimulus (27). We investigated whether the theta rhythm described above for V1 and V4 modulates gamma power, and whether this is affected by selective attention. As described above, we found that theta is spatially coextensive with visually induced gamma and reduced by attention. Therefore, to explore whether theta phase modulates gamma amplitude, we first selected conditions with maximal theta strength, that is, visual stimulation with a non-attended stimulus. Figure 6A shows for one example electrode the raw spectral power as a function of time relative to the theta trough. This reveals that the amplitude of visually induced gamma-band power is modulated systematically by theta phase. Figure 6B shows the resulting PAC, averaged over all electrodes in V1 and V4, and over both attentional conditions. It reveals a distinct peak of PAC between theta phase and gamma power. We note that the theta-rhythmic modulation of gamma was most pronounced for the high-frequency end of the gamma band. In addition, this analysis reveals PAC between the phase around 1 Hz and power in several frequency bands; this 1 Hz component is likely related to the temporal frequency of the drifting gratings (see Materials and Methods).

Figure 7 shows PAC separately for areas V1 and V4 and for the two attention conditions. In V1, there was a PAC peak for phase-frequencies around 4 Hz (Fig. 7A,B). This theta-gamma PAC was strongly reduced by attention (Fig. 7C). There were additional significant PAC components at lower phase frequencies, which partly also showed significant attentional effects. As mentioned above, these slower components are likely related to the temporal frequency of the drifting gratings. In contrast to V1, V4 did not show significant theta-gamma PAC, and also no significant PAC difference between attention conditions (Fig. 7D-F).

Visual theta remains after microsaccade removal. It has previously been shown that theta-band rhythmicity is present in the sequence of microsaccades (MSs) (31, 32). MSs cause a movement of the retinal image and an MS-related response in the LFP and the multi-unit activity (31). MSs also modulate the strength of gamma-band activity (31, 32). Thus, the MS rhythm may underlie both the theta rhythm and the theta-gamma PAC observed here. To investigate this, we first quantified the phase-locking between MSs and the LFP in V1. Figure 8A shows the MS-LFP PPC spectrum and reveals a clear theta peak. If neuronal activity and phase locking in the theta band were due to driving by theta-rhythmic MSs, then removal of epochs with MSs should diminish the observed theta rhythmicity. To test this, we excluded MSs with increasing stringency and investigated the effect on the observed neuronal theta rhythmicity. We detected MSs and excluded data recorded between MS onset and 0.5 s thereafter. This substantially reduced the amount of available data. We calculated low-frequency PPC spectra within V1 for the attend-away condition for 1) all available epochs (N=1917 epochs), 2) epochs excluding MSs exceeding average eye speed by 5 SD (N=827 epochs), 3) epochs excluding MSs exceeding average eye speed by 3 SD (N=446 epochs). Figure 8B reveals that excluding MSs with increasing stringency did not decrease theta rhythmicity in V1. These results strongly suggest that, while there is phase locking between MSs and cortical theta, the cortical theta exists independently of the occurrence of MSs (31). Figure 9 investigates the influence of MS removal (at 5 SD to retain acceptable statistical sensitivity) on further metrics of visual theta. The main results remained essentially unchanged: Low-frequency power spectra (after robust regression of $1/f^n$ and removal) show theta peaks for attention ipsilateral, which are reduced by attention to the contralateral stimulus (Fig. 9A,B); PPC spectra show theta peaks for all cases (Fig. 9C-E), and significant attentional reduction; PAC in area V1 shows a peak for theta-band phase frequencies and gamma-band amplitude frequencies only when attention is directed to the ipsilateral stimulus (Fig. 9F,G,H). When we excluded MSs exceeding average eye speed by merely 3 SD, i.e. when we applied an even more stringent MS removal, the results remained qualitatively unchanged (data not shown). Only the reduction of theta-band V1-V4 PPC with attention did not any more reach significance, probably due to strongly reduced statistical sensitivity.

Control for microsaccade rate. In addition, we performed an alternative control, by equating the MS rate, that is, the MS temporal density, between attention conditions. This specifically controls for potential MS rate differences between attention conditions. Figure 9A shows the cumulative distribution of MS rate over the respective number of data epochs (see Materials and Methods for MS rate estimation). MS rate actually differed between attention conditions. We therefore stratified the data (see Materials and Methods) to arrive at two equally sized sets of epochs with an essentially equal distribution of MS rates (dashed lines in Fig. 9A). After stratification, almost all main results remained essentially unchanged (Fig. 9B-G). Note that V4 theta power (after robust regression of $1/f^n$ and removal) did not show a significant attentional effect, yet such an effect was significant for V4-V4 PPC. When we stratified based

on MSs detected by a 3 SD threshold, all results remained qualitatively the same as without stratification.

Control for theta power. Finally, we controlled for the possibility that the effects of attention on theta PPC, theta GC or theta-gamma PAC were explained by the effects of attention on theta power. Specifically, theta power was enhanced with ipsilateral attention, which might enhance the sensitivity of PPC, GC and/or PAC quantification, which might in turn explain the enhanced PPC, GC and/or PAC values with ipsilateral attention. To investigate this possibility, we stratified for theta power between attention conditions. After stratification, attention conditions did not any more differ significantly in either theta PPC (V1-V1, V4-V4 or V1-V4), theta GC (V1-to-V4 or V4-to-V1) or theta-gamma PAC (in V1 or V4). This is consistent with two interpretations. One interpretation relates to the signal-to-noise ratio (SNR) of theta. The enhanced theta power in the attend-away condition might increase the sensitivity of the theta PPC and the theta-gamma PAC quantification and thereby explain the attention effect on those metrics. An alternative interpretation relates to the relative amount of time with strong theta power. The enhanced theta power in the attend-away condition might correspond to more time spent in a regime of strong theta rhythmicity. This might conceivably be a genuine difference between attention conditions. If this is the case, stratification for theta power artificially removes this genuine difference. There is no unequivocal way to distinguish between these two interpretations.

Note that the increased theta power in the attend-away condition most likely reflects an increased theta-rhythmic synchronization among local neurons. In general, power increases can be due to increases in synchronization or increases in the activity of the involved neurons. However, V1 and V4 neurons, when activated with one stimulus in their RFs as done here, show neuronal activity that increases with attention or stays unchanged (54).

Discussion

We demonstrated the presence of a ≈4 Hz theta rhythm in awake macaque V4 and V1. This theta rhythm was present selectively in sites driven by the visual stimulus, such that the spatial map of theta co-extended with the map of visually induced gamma-band activity. In V1, theta rhythmically modulated local gamma-band activity and thereby most likely the gamma-associated local processing of visual information. Theta rhythms in V1 and V4 synchronized, and an analysis of GC revealed a predominant feedforward influence. Theta rhythmicity was substantially reduced by selective attention to a visual stimulus contralateral to the recorded areas. Visual cortical theta showed phase locking with MSs. Yet, exclusion of MS effects left all main theta-related observations essentially unchanged.

We were somewhat surprised to find that theta shows a clear spatial correlation or coextension with visually induced gamma-band power. There were reasons to assume that a putative theta rhythm might be global across visual cortex. Hippocampal recordings suggest that theta is global in this structure, travelling as a wave from dorsal to ventral parts (55, 56). Also, there is the general notion that slower rhythms are more global than faster rhythms (57,

58). Yet, our finding of a spatially specific theta, which is coupled to gamma by spatial extension and also through PAC, is also in agreement with one previous study: Inter-areal GC influences in both theta and gamma are typically stronger in the anatomically defined feedforward than feedback direction (30).

The PAC analysis showed theta-gamma coupling that peaked for an amplitude-frequency at the high-frequency end of the visually induced gamma band activity. Thus, theta-rhythmic modulation was most apparent for this high-frequency part of the overall gamma peak. This might reflect a physiological asymmetry or be related to signal-to-noise ratio. Physiologically, it is conceivable that the modulation is in fact stronger at the upper flank of the gamma peak than at the lower flank, which would be equivalent to an asymmetric broadening of the gamma peak towards higher frequencies. Alternatively, the gamma-band peak is modulated in its entirety, yet the PAC metric ends up larger for the upper than the lower flank, e.g. because the gamma peak is superimposed on unmodulated (or less modulated) $1/f^n$ power. If we consider the $1/f^n$ component of the power spectrum as noise, this noise is larger for the lower than the upper flank.

In addition, it is interesting to investigate the precise frequency of the observed theta rhythm. The basic spectra of power (residuals) and phase locking showed peaks close to 4 Hz. The analysis of spatial correlation between theta power and visually-induced gamma power showed a broader peak that includes 4 Hz, yet extends up to 8 Hz. This suggests that the underlying phenomenon might actually occupy this broader frequency range, with theta merely peaking at 4 Hz for the particular stimulus and task conditions used here. Whether other stimuli or tasks make theta in V1 and/or V4 shift in frequency is an interesting topic for further study. In any case, the 4-8 Hz range found in the spatial correlation analysis is an interesting link to the classical hippocampal theta, which occupies this range. Hippocampal theta in fact shifts in frequency, e.g. depending on running speed (62, 63).

The mechanisms behind the observed visual cortical theta rhythm and its attentional modulation are not yet clear. The mechanisms underlying hippocampal theta have been studied in great detail (64), and hippocampal theta is partly synchronized to neocortex, e.g. to entorhinal and prefrontal areas. It is conceivable that this theta synchronizes further to intermediate and lower visual areas, yet we deem it unlikely that this is the source of the theta observed here. Such a mechanism would most likely not generate the spatial coextension between theta and gamma, and the predominant GC direction from V1 to V4, which we observed here. The present results place further constraints on potential mechanisms: The fact that removing MSs left the main results essentially unchanged suggests that theta in visual cortex does not merely reflect theta-rhythmic MSs. Rather, the clear spatial co-extension between theta power and visually induced gamma suggests a role for visually driven activity in theta generation.

The theta rhythms in V1 and V4 were reduced by selective attention to a contralateral stimulus. Attention effects are typically smaller in V1 than in higher visual areas (for otherwise comparable conditions). This holds for firing rates (54, 59) and gamma-band synchronization (60). In fact, for gamma-band synchronization, different studies in V1 have reported attentional increases (60), decreases (61) or the absence of an effect (29). By contrast, the

attentional effects on theta appeared to be of similar strength in V4 and V1, entailing an unusually strong attention effect for V1.

Many studies have reported reductions in alpha power at the neuronal representation of visual stimuli or visual attention (28, 65). The attentional reduction of theta observed here might be a related phenomenon at a slightly lower frequency. However, whereas visually driven neuronal ensembles show reduced alpha (28), we found that they show enhanced theta (Fig. 4). This observation supports an alternative scenario. Recent studies have shown that attention samples visual stimuli at a theta rhythm. When human subjects have to detect the appearance of a faint stimulus at a peripheral location, their detection performance is modulated by the phase of a 7-8 Hz rhythm with a maximum over frontal cortex (66). This might reflect an ≈8 Hz rhythmic attentional sampling. In support of this, three subsequent studies have shown that two simultaneously monitored stimuli are attentionally sampled in alternation, each at ≈4 Hz (67-69). A further study estimated the temporal sampling frequency of attention, and found it to be around 7 Hz for a single attended stimulus, 4 Hz for two and 2.6 Hz for three (70). These numbers are consistent with a single attentional sampling mechanism that is multiplexed over the to-be-attended stimuli. Such a scenario would also explain theta-rhythmic modulations of firing rates in inferotemporal (IT) cortex during the presentation of two stimuli (26). When IT neurons respond to one stimulus, and a second stimulus is added onto the screen, firing rates start oscillating at ≈4 Hz in a way that suggests that attention is drawn to the newly presented stimulus and subsequently alternates between the two stimuli. At first glance, these results might seem to suggest that visual cortical theta should be stronger for the attended stimulus, in contrast to our findings. Yet, the fact that divided attention tasks reveal theta-rhythmic sampling does not mean that attended stimuli are affected by stronger theta-rhythmic modulation than non-attended stimuli. The mentioned recordings in IT showed strong theta rhythmicity when two stimuli were presented, but weaker theta rhythmicity when a single stimulus was presented and thereby received full attention. Based on these and the present results, we propose that attention is more sustained, yet still weakly theta rhythmic, at the attended location, and that it theta-rhythmically scans the space around it, to explore other stimuli. As a consequence, non-attended stimuli receive attentional processing benefits only when they are attentionally scanned, leading to relatively strong theta rhythmicity. This scanning hypothesis is consistent with theta-rhythmic modulations of detection performance when one location on an extended stimulus is attended, while another location on the same object is not attended: The non-attended location is consistently sampled at an 8 Hz rhythm, yet with a 90 degree phase offset in the 8 Hz cycle to the attended location (69).

Future studies will need to investigate whether attentional control structures show an ≈8 Hz sampling rhythm that is coherent to the sampled stimulus representations in visual cortex. As mentioned above, the ≈8 Hz EEG component, whose phase predicts human detection performance, is strongest over frontal areas (66). Also, spike and LFP recordings in macaque parietal cortex have recently revealed a similar theta rhythm (21, 22). If such theta-rhythmic top-down influences were to be found, it will be interesting to understand how they fit with the predominantly bottom-up directed theta influences observed between visual areas (30).

One possibility is that control structures exert a theta-rhythmic perturbation on early and even primary visual cortex, which then percolates up through the hierarchy of visual areas.

Materials and Methods

Subjects, stimuli and task. Two adult male macaque monkeys participated in this study. All procedures were in accordance with Dutch and European regulations for the protection of animals and were approved by the animal ethics committee of Radboud University Nijmegen (Netherlands). The data analyzed here have been (partially) used in previous studies (29, 30, 33-40).

Stimuli and behavior were controlled by the software CORTEX (http://dally.nimh.nih.gov). Stimuli were presented on a CRT monitor at 120 Hz non-interlaced. When the monkey touched a bar, a gray fixation point appeared at the center of the screen. When the monkey brought its gaze into a fixation window around the fixation point (0.85 degree radius in monkey K; 1 deg radius in monkey P), a pre-stimulus baseline of 0.8 s started. If the monkey's gaze left the fixation window at any time, the trial was terminated. The measured eye positions during correct trials used for analysis differed only by an average of 0.03 deg of visual angle between the two attention conditions. After the baseline period, two physically isoluminant patches of drifting sinusoidal grating appeared (diameter= 3 degrees, spatial frequency ≈1 cycles/degree, drift velocity ≈1 degree/s, resulting temporal frequency ≈1 cycle/s, contrast= 100%). The two grating patches chosen for a given recording session always had equal eccentricity, size, contrast, spatial frequency and drift velocity. The two gratings always had orientations that were orthogonal to each other, and they had drift directions that were incompatible with a Chevron pattern moving behind two apertures, to avoid pre-attentive binding. In any given trial, one grating was tinted yellow, the other blue, with the color assigned randomly across trials. The yellow and blue colors were physically equiluminant. After 1-1.5 s (0.8-1.3 s in monkey P), the fixation point changed color to match the color of one of the two gratings, thereby indicating this grating as the relevant stimulus and the other as irrelevant. For each trial, two independent change times for the two stimuli were determined randomly between stimulus onset and 4.5 s after cue onset, according to a slowly rising hazard rate. If the relevant stimulus changed (before or after the irrelevant stimulus changed), and the monkey released the bar within 0.15-0.5 s thereafter, the trial was terminated and a reward was given. If the monkey released the bar at any other time, the trial was terminated without reward. The stimulus changes were small changes in the grating pattern, with the stripes undergoing a gentle bend. During the bend, the outer ends of the grating stripes lagged increasingly behind the center of the stripes, until the lag reached 0.1 degree at 75 ms after the start of the bend. Over the course of another 75 ms, the stripes straightened again.

Several sessions (either separate or after attention-task sessions) were devoted to the mapping of receptive fields (RFs), using 60 patches of moving grating. Receptive field positions were stable across recording sessions (29).

Neurophysiological recordings and signal preprocessing. Neuronal recordings were made from two left hemispheres in two monkeys through a micromachined 252-channel electrocorticographic electrode array (ECoG) implanted subdurally. The details of the production and the electrochemical properties have been described in a separate paper (41). Briefly, ECoG grids were 10 micron thick polyimide foils with 0.3 micron thick Platinum electrodes and conductive lanes embedded. Electrodes had an exposed surface with a diameter of 1 mm and a center-to-center spacing of 2-3 mm. Electrodes were arranged in lanes, and two neighboring lanes ran parallel on one "finger" of the polyimide foil (30). The structuring in separate fingers avoided wrinkling of the ECoG on the brain surface and corresponding pressure points. For ECoG implantation, a 6.5x4 cm craniotomy over the left hemisphere in each monkey was performed under aseptic conditions with isoflurane anesthesia. The dura was opened and the ECoG was placed directly onto the brain under visual control. Several high resolution photos were taken before and after placement of the ECoG for later coregistration of ECoG signals with brain regions. After ECoG implantation, both the bone and the dural flap were placed back and secured in place. After a recovery period of approximately three weeks, we started with neuronal recordings.

Signals obtained from the 252-electrode grid were amplified 20 times by eight Plexon headstage amplifiers (Plexon, USA), high-pass filtered at 0.159 Hz, low-pass filtered at 8 kHz and digitized at 32 kHz by a Neuralynx Digital Lynx system (Neuralynx, USA). LFP signals were obtained by low-pass filtering at 200 Hz and downsampling to 1 kHz. Powerline artifacts were removed by digital notch filtering. The actual spectral data analysis included spectral smoothing that rendered the original notch invisible.

Data analysis general. All analyses were done in MATLAB (The MathWorks, USA) and using FieldTrip (42) (http://fieldtrip.fcdonders.nl).

Recording electrodes versus recording sites. During recordings, all ECoG electrodes were referenced against one silver ball implanted epidurally over the other hemisphere. This common reference could lead to artifactual correlations between the signals of separate electrodes. Therefore, all metrics of interaction between distant groups of neurons, that is the pairwise phase consistency (PPC) and Granger causality (GC), were applied after removing the common reference by local bipolar differentiation. That is, the signals from two immediately neighboring electrodes were subtracted from each other. We refer to the ECoG contacts as "electrodes" and to the local bipolar derivations as "recording sites" or just "sites". All analyses of local neuronal activity used directly the signals recorded from the electrodes, to minimize preprocessing and to minimize reduction in theta amplitude due to theta phase alignment between neighboring electrodes.

Selection of electrodes and sites. The ECoG grids provided dense coverage of dorsal V1, the superficial part of dorsal V2, dorsal V4 and posterior TEO (29, 30). For simplicity, we refer to V1 and V2 sites as V1, and to V4 and TEO sites as V4. Monkey K had 45 electrodes on V1,

resulting in 40 bipolar sites, and 24 electrodes on V4, resulting in 19 sites. Monkey P had 72 electrodes on V1, resulting in 64 sites, and 26 electrodes on V4, resulting in 21 sites.

Normalization of signals across electrodes and recording sessions. Signal amplitude could vary across electrodes because several separate headstages were used. Furthermore, signal amplitude of a given electrode could vary across sessions, probably due to variable quality of contact to the cortical surface. To equalize the contribution of different electrodes and sessions, we applied a z-transform: For each electrode and session, the raw LFP signal was demeaned and divided by its standard deviation.

Segmenting data into epochs. Each successfully completed trial contained three periods: The pre-stimulus, the pre-cue and the post-cue period. The pre-stimulus period was the time between fixation onset and stimulus onset. During the pre-stimulus period, monkeys fixated on a fixation point on a gray screen, and there was no stimulus presented and no cue had been nor was presented during that time. The pre-cue period was the time between stimulus onset and cue onset. During the pre-cue period, monkeys kept fixation, the stimuli were continuously present, one tinted yellow the other blue, chosen randomly, and the fixation point had not yet assumed a color, and thereby the attentional cue had not been given. The post-cue period was the time between cue onset and target change. During the post-cue period, monkeys kept fixation, the stimuli were continuously present with their tints and the fixation point was tinted in one of these colors, thereby providing the attentional cue. On approximately half of the trials, the post-cue period contained a distracter change, and the data immediately following this event were excluded as explained below. The pre-stimulus, pre-cue and post-cue periods all were of variable length across trials. The spectral analysis was based on epochs of fixed lengths. Therefore, the described task periods were cut into non-overlapping epochs. We aimed at excluding data soon after events, like stimulus onset, cue onset and distracter change, to minimize effects of post-event transients and non-stationarities on the metrics of rhythmicity and synchronization. Therefore, periods were cut into non-overlapping epochs, starting from the end of the period and stopping, before an epoch would have included data less than 0.5 s after those events. In general, we cut epochs of 1 s length, to achieve a fundamental spectral resolution (Rayleigh frequency) of one Hertz. This was used for the analysis of PPC, GC and phase-amplitude coupling (PAC). The PAC analysis required the prior estimation of the power time course, for which we employed window lengths of ±2.5 cycles per frequency. In this case, epochs were cut such that the power estimation windows excluded data less than 0.5 s after events. The estimation of power spectra was based on 1.6 s epochs, because theta peaks were visible but less conspicuous when 1 s epochs were used.

Spectral estimation. Epochs were Hann tapered and Fourier transformed. For the PAC analysis, the ±2.5 cycle long windows were also treated in this way. For the analysis of the spatial correlation between theta power and stimulus induced gamma power, the gamma-power estimation used multitaper spectral estimation with seven tapers taken from the discrete prolate spheroidal sequence, defined on 0.5 s long epochs (43).

Robust regression. We reduced the $1/f^n$ background in power spectra by estimating the $1/f^n$ component and subtracting it. Specifically, for each electrode separately, we pooled attention conditions and fitted a line to the log-log power plot between 0.625 and 10 Hz, using robust regression as implemented in the MATLAB "robustfit" function with default settings. Robust regression uses an iterative procedure that lends less weight to data that are far from the fitted function. Subsequently, the fitted line was subtracted to obtain the power residuals.

Pairwise phase consistency (PPC) and Phase-amplitude coupling (PAC). Phase locking was quantified with the pairwise phase consistency (PPC) metric (44). We used PPC both to quantify the locking between LFPs recorded from separate sites, the locking between microsaccades and LFP, and the locking between the LFP phase and its amplitude fluctuations, that is, the PAC (phase-amplitude coupling) (45). PPC is not biased by the number of epochs, whereas the more conventional coherence metric has that bias. Essentially, the PPC calculation proceeds in two steps. First, the relative phases are calculated for the multiple epochs of the two signals. The second step is the crucial step: In conventional coherence calculation, those relative phases are averaged, which leads to the bias by epoch number; in PPC calculation, all possible pairs of relative phases are formed, the cosines between those relative phases are determined and those cosine values are averaged.

To quantify PAC, we computed the PPC between the LFP at lower frequencies, the "phase-frequencies", and the time-varying power at higher frequencies, the "amplitude-frequencies". One-second long epochs of the raw LFP and of its time-varying power were Fourier transformed, and locking among the phase estimates at the phase-frequencies was quantified as the PPC across all available epochs. PAC can in general only be estimated for pairs of phase- and amplitude-frequencies, for which the amplitude frequency is higher than the phase frequency. In addition, the estimation of time-varying power entails low-pass filtering, and PAC can only be estimated for pairs of phase- and amplitude-frequencies, for which this low-pass frequency is above the phase frequency. Power is estimated on the basis of epochs and tapers of finite length. As described above, we chose epochs of ±2.5 cycle length per frequency. In order to assess the resulting low-pass filtering, we applied the power estimation 10000 times to a random Gaussian process of the same length as the data epochs, and determined the frequency, at which this low-pass filtering reduced the average power to less than 70% of the power in the passband. For example, for 50 Hz, this cutoff frequency was 7.7 Hz. This procedure was applied for each amplitude frequency, and the PAC for this amplitude frequency was only considered up to the respective phase frequency. The excluded combinations of phase-frequencies and amplitude-frequencies are masked with black in the figures. The PAC results shown here use phase and power estimates from the same electrode. We also calculated PAC by combining phase estimates from one electrode with power estimates of neighboring electrodes, and this left the results essentially unchanged.

Granger causality. We used the non-parametric estimation of Granger causality (46). For this, Fourier spectra were estimated as described above and entered into a non-parametric spectral matrix factorization (NPSF) as implemented in the FieldTrip toolbox.

Statistical testing. The confidence intervals shown for power and PPC spectra in Figure 1 were estimated with a bootstrap procedure (1000 bootstrap replications for power, 500 for PPC) (47): Spectra were first averaged across electrodes (for power) or site pairs (for PPC), and subsequently, the bootstrap was performed across epochs. All statistical comparisons were based on non-parametric permutation and included corrections for the multiple comparisons made across frequencies. We illustrate the procedure for the comparison of power between the two attention conditions. The power difference between the attention conditions was first averaged over all electrodes per monkey and then over the two animals, giving the observed power difference per frequency. Subsequently, the following procedure was done 1000 times: 1) The attention conditions were randomly exchanged between epochs, keeping the original number of epochs per attention conditions constant; 2) The average power difference was calculated as described for the observed data; 3) The maximal (minimal) difference across all frequencies was placed into the randomization distribution of maximal (minimal) values; 4) The 2.5^{th} percentile of the minimal values and the 97.5^{th} percentile of the maximal values were taken as statistical thresholds. The observed differences were compared to those thresholds. This procedure implements a non-parametric version of a two-sided test with multiple comparison correction (48). The same procedure was used for comparing power, PPC, GC and PAC values between attention conditions; for power and PAC, we used 1000 permutations, for PPC and GC 500 permutations.

The spatial correlation coefficients and the PAC values were tested in two ways: They were compared between attention conditions as described, and they were additionally tested for the presence of significant correlation or PAC. In the case of PAC, the comparison was done between the observed values and a randomization distribution obtained by randomly pairing raw LFP epochs and power time courses 1000 times. After each random pairing and recalculation of PAC, maximal and minimal values across all frequency-frequency pairs were placed into the respective randomization distribution, and further testing proceeded as described. In the case of the spatial correlations, the comparison was done between the observed values and zero, because the Spearman rank correlation has no bias; the randomization was done by randomly pairing electrodes between the theta power residuals and the stimulus induced gamma. After each randomization, maximal and minimal correlation values across all tested frequencies were placed into the respective randomization distribution, and further testing proceeded as described.

Microsaccade detection. Raw vertical and horizontal eye position signals were low-pass filtered by replacing each value with the average over itself ±15 samples (at 1 kHz sampling rate). Signals were then differentiated in time to obtain the vertical and horizontal velocities. Those are combined to obtain the eye speed irrespective of the direction of eye movement. Per trial, the standard deviation of eye speed was determined, and any deviation larger than 5 SDs and lasting for at least 30 ms was considered a saccadic eye movement. Saccadic eye movements that remained within the fixation window were considered microsaccades (MSs).

Stratification. We intended to test, whether some of the observed differences were due to differences in the rate of MSs, which existed between attention conditions, or in the power of theta, which existed between attention conditions or between areas. To this end, we used a stratification approach, that is, we randomly subsampled the available data to equate as well as possible the distributions of MS rates or theta power (49). For MS stratification, we first calculated MS density by convolving the MS sequence with a Gaussian kernel with an SD of 150 ms (truncated at ±500 ms). For each epoch, we calculated the average MS density, which was then used for stratification. For theta power stratification, we estimated and removed the $1/f^n$ component for each electrode, averaged over electrodes, and used the resulting average residual theta (3-5 Hz) power for stratification. We describe the stratification procedure for a given parameter (MS density or theta power) for the attention contrast: The parameter distributions were compiled for the two attention conditions and binned into 40 equally spaced bins. For each bin, the number of entries for the two attention conditions was equated by random subsampling with a procedure that aims at equating the parameter averages between the conditions as well as possible. This procedure is applied to the distributions per bin: 1) The condition with more entries is defined as the larger condition, the other as the smaller condition; 2) The mean of the parameter for the smaller condition is calculated and taken as target value; 3) The larger condition is randomly subsampled, by first drawing one entry at random, and then proceeding as follows: a) A further entry is randomly drawn; b) If the mean of the current bin entries (or the starter entry) is smaller (larger) than the target value, the new entry is added if it is larger (smaller), otherwise it is discarded and a new random draw is performed. This latter step aims at equating means; if no such entry is present, a randomly drawn entry is accepted. Stratification across areas proceeded accordingly.

Acknowledgements:

PF acknowledges grant support by DFG (SPP 1665, FOR 1847, FR2557/5-1-CORNET), EU (HEALTH-F2-2008-200728-BrainSynch, FP7-604102-HBP, FP7-600730-Magnetrodes), a European Young Investigator Award, NIH (1U54MH091657-WU-Minn-Consortium-HCP), and LOEWE (NeFF). The authors thank Jarrod Dowdall for help with microsaccade detection and Martin Vinck for helpful comments on the manuscript.

References

1. Buzsáki G (2006) *Rhythms of the brain* (Oxford University Press, Oxford ; New York) pp xiv, 448 p.
2. Keitel A & Gross J (2016) Individual Human Brain Areas Can Be Identified from Their Characteristic Spectral Activation Fingerprints. *PLoS biology* 14(6):e1002498.
3. O'Keefe J & Recce ML (1993) Phase relationship between hippocampal place units and the EEG theta rhythm. *Hippocampus* 3(3):317-330.
4. Hafting T, Fyhn M, Bonnevie T, Moser MB, & Moser EI (2008) Hippocampus-independent phase precession in entorhinal grid cells. *Nature* 453(7199):1248-1252.
5. Jezek K, Henriksen EJ, Treves A, Moser EI, & Moser MB (2011) Theta-paced flickering between place-cell maps in the hippocampus. *Nature* 478(7368):246-249.
6. Skaggs WE, McNaughton BL, Wilson MA, & Barnes CA (1996) Theta phase precession in hippocampal neuronal populations and the compression of temporal sequences. *Hippocampus* 6(2):149-172.
7. Dragoi G & Buzsaki G (2006) Temporal encoding of place sequences by hippocampal cell assemblies. *Neuron* 50(1):145-157.
8. Kahana MJ, Sekuler R, Caplan JB, Kirschen M, & Madsen JR (1999) Human theta oscillations exhibit task dependence during virtual maze navigation. *Nature* 399(6738):781-784.
9. Killian NJ, Jutras MJ, & Buffalo EA (2012) A map of visual space in the primate entorhinal cortex. *Nature* 491(7426):761-764.
10. Jutras MJ, Fries P, & Buffalo EA (2013) Oscillatory activity in the monkey hippocampus during visual exploration and memory formation. *Proceedings of the National Academy of Sciences of the United States of America* 110(32):13144-13149.
11. Rutishauser U, Ross IB, Mamelak AN, & Schuman EM (2010) Human memory strength is predicted by theta-frequency phase-locking of single neurons. *Nature* 464(7290):903-907.
12. Lega BC, Jacobs J, & Kahana M (2012) Human hippocampal theta oscillations and the formation of episodic memories. *Hippocampus* 22(4):748-761.
13. Axmacher N*, et al.* (2010) Cross-frequency coupling supports multi-item working memory in the human hippocampus. *Proceedings of the National Academy of Sciences of the United States of America* 107(7):3228-3233.
14. Raghavachari S*, et al.* (2001) Gating of human theta oscillations by a working memory task. *The Journal of neuroscience : the official journal of the Society for Neuroscience* 21(9):3175-3183.
15. Siapas AG, Lubenov EV, & Wilson MA (2005) Prefrontal phase locking to hippocampal theta oscillations. *Neuron* 46(1):141-151.
16. Sirota A*, et al.* (2008) Entrainment of neocortical neurons and gamma oscillations by the hippocampal theta rhythm. *Neuron* 60(4):683-697.
17. Brincat SL & Miller EK (2015) Frequency-specific hippocampal-prefrontal interactions during associative learning. *Nature neuroscience* 18(4):576-581.
18. Debener S*, et al.* (2005) Trial-by-trial coupling of concurrent electroencephalogram and functional magnetic resonance imaging identifies the dynamics of performance monitoring. *The Journal of neuroscience : the official journal of the Society for Neuroscience* 25(50):11730-11737.
19. Voloh B, Valiante TA, Everling S, & Womelsdorf T (2015) Theta-gamma coordination between anterior cingulate and prefrontal cortex indexes correct attention shifts. *Proceedings of the National Academy of Sciences of the United States of America* 112(27):8457-8462.
20. Babapoor-Farrokhran S, Vinck M, Womelsdorf T, & Everling S (2017) Theta and beta synchrony coordinate frontal eye fields and anterior cingulate cortex during sensorimotor mapping. *Nature communications* 8:13967.
21. Hawellek DJ, Wong YT, & Pesaran B (2016) Temporal coding of reward-guided choice in the posterior parietal cortex. *Proceedings of the National Academy of Sciences of the United States of America* 113(47):13492-13497.
22. Phillips JM, Vinck M, Everling S, & Womelsdorf T (2014) A long-range fronto-parietal 5- to 10-Hz network predicts "top-down" controlled guidance in a task-switch paradigm. *Cereb Cortex* 24(8):1996-2008.
23. Womelsdorf T, Johnston K, Vinck M, & Everling S (2010) Theta-activity in anterior cingulate cortex predicts task rules and their adjustments following errors. *Proceedings of the National Academy of Sciences of the United States of America* 107(11):5248-5253.
24. Liebe S, Hoerzer GM, Logothetis NK, & Rainer G (2012) Theta coupling between V4 and prefrontal cortex predicts visual short-term memory performance. *Nature neuroscience* 15(3):456-462, S451-452.

25. Lee H, Simpson GV, Logothetis NK, & Rainer G (2005) Phase locking of single neuron activity to theta oscillations during working memory in monkey extrastriate visual cortex. *Neuron* 45(1):147-156.
26. Rollenhagen JE & Olson CR (2005) Low-frequency oscillations arising from competitive interactions between visual stimuli in macaque inferotemporal cortex. *Journal of neurophysiology* 94(5):3368-3387.
27. Esghaei M, Daliri MR, & Treue S (2015) Attention Decreases Phase-Amplitude Coupling, Enhancing Stimulus Discriminability in Cortical Area MT. *Frontiers in neural circuits* 9:82.
28. Fries P, Womelsdorf T, Oostenveld R, & Desimone R (2008) The effects of visual stimulation and selective visual attention on rhythmic neuronal synchronization in macaque area V4. *The Journal of neuroscience : the official journal of the Society for Neuroscience* 28(18):4823-4835.
29. Bosman CA*, et al.* (2012) Attentional stimulus selection through selective synchronization between monkey visual areas. *Neuron* 75(5):875-888.
30. Bastos AM*, et al.* (2015) Visual areas exert feedforward and feedback influences through distinct frequency channels. *Neuron* 85(2):390-401.
31. Bosman CA, Womelsdorf T, Desimone R, & Fries P (2009) A microsaccadic rhythm modulates gamma-band synchronization and behavior. *The Journal of neuroscience : the official journal of the Society for Neuroscience* 29(30):9471-9480.
32. Lowet E, Roberts MJ, Bosman CA, Fries P, & De Weerd P (2016) Areas V1 and V2 show microsaccade-related 3-4-Hz covariation in gamma power and frequency. *The European journal of neuroscience* 43(10):1286-1296.
33. Bastos AM*, et al.* (2015) A DCM study of spectral asymmetries in feedforward and feedback connections between visual areas V1 and V4 in the monkey. *NeuroImage* 108:460-475.
34. Brunet N*, et al.* (2015) Visual cortical gamma-band activity during free viewing of natural images. *Cereb Cortex* 25(4):918-926.
35. Brunet N, Vinck M, Bosman CA, Singer W, & Fries P (2014) Gamma or no gamma, that is the question. *Trends in cognitive sciences* 18(10):507-509.
36. Brunet NM*, et al.* (2014) Stimulus repetition modulates gamma-band synchronization in primate visual cortex. *Proceedings of the National Academy of Sciences of the United States of America* 111(9):3626-3631.
37. Lewis CM, Bosman CA, Womelsdorf T, & Fries P (2016) Stimulus-induced visual cortical networks are recapitulated by spontaneous local and interareal synchronization. *Proceedings of the National Academy of Sciences of the United States of America* 113(5):E606-615.
38. Pinotsis DA*, et al.* (2014) Contrast gain control and horizontal interactions in V1: A DCM study. *NeuroImage*.
39. Richter CG, Thompson WH, Bosman CA, & Fries P (2015) A jackknife approach to quantifying single-trial correlation between covariance-based metrics undefined on a single-trial basis. *NeuroImage* 114:57-70.
40. Vinck M*, et al.* (2015) How to detect the Granger-causal flow direction in the presence of additive noise? *NeuroImage* 108:301-318.
41. Rubehn B, Bosman C, Oostenveld R, Fries P, & Stieglitz T (2009) A MEMS-based flexible multichannel ECoG-electrode array. *Journal of neural engineering* 6(3):036003.
42. Oostenveld R, Fries P, Maris E, & Schoffelen JM (2011) FieldTrip: Open source software for advanced analysis of MEG, EEG, and invasive electrophysiological data. *Computational intelligence and neuroscience* 2011:156869.
43. Mitra PP & Pesaran B (1999) Analysis of dynamic brain imaging data. *Biophysical journal* 76(2):691-708.
44. Vinck M, van Wingerden M, Womelsdorf T, Fries P, & Pennartz CM (2010) The pairwise phase consistency: a bias-free measure of rhythmic neuronal synchronization. *NeuroImage* 51(1):112-122.
45. Scheffer-Teixeira R & Tort AB (2016) On cross-frequency phase-phase coupling between theta and gamma oscillations in the hippocampus. *eLife* 5.
46. Dhamala M, Rangarajan G, & Ding M (2008) Estimating Granger causality from fourier and wavelet transforms of time series data. *Physical review letters* 100(1):018701.
47. Efron B & Tibshirani RJ (1994) *An introduction to the bootstrap* (CRC Press).
48. Nichols TE & Holmes AP (2002) Nonparametric permutation tests for functional neuroimaging: a primer with examples. *Hum Brain Mapp* 15(1):1-25.
49. Schoffelen JM, Oostenveld R, & Fries P (2005) Neuronal coherence as a mechanism of effective corticospinal interaction. *Science* 308(5718):111-113.
50. Vinck M, Womelsdorf T, Buffalo EA, Desimone R, & Fries P (2013) Attentional modulation of cell-class-specific gamma-band synchronization in awake monkey area V4. *Neuron* 80(4):1077-1089.

51. Fries P, Reynolds JH, Rorie AE, & Desimone R (2001) Modulation of oscillatory neuronal synchronization by selective visual attention. *Science* 291(5508):1560-1563.
52. Manning JR, Jacobs J, Fried I, & Kahana MJ (2009) Broadband shifts in local field potential power spectra are correlated with single-neuron spiking in humans. *The Journal of neuroscience : the official journal of the Society for Neuroscience* 29(43):13613-13620.
53. Bragin A*, et al.* (1995) Gamma (40-100 Hz) oscillation in the hippocampus of the behaving rat. *The Journal of neuroscience : the official journal of the Society for Neuroscience* 15(1 Pt 1):47-60.
54. Luck SJ, Chelazzi L, Hillyard SA, & Desimone R (1997) Neural mechanisms of spatial selective attention in areas V1, V2, and V4 of macaque visual cortex. *Journal of neurophysiology* 77(1):24-42.
55. Lubenov EV & Siapas AG (2009) Hippocampal theta oscillations are travelling waves. *Nature* 459(7246):534-539.
56. Patel J, Fujisawa S, Berenyi A, Royer S, & Buzsaki G (2012) Traveling theta waves along the entire septotemporal axis of the hippocampus. *Neuron* 75(3):410-417.
57. von Stein A & Sarnthein J (2000) Different frequencies for different scales of cortical integration: from local gamma to long range alpha/theta synchronization. *International journal of psychophysiology : official journal of the International Organization of Psychophysiology* 38(3):301-313.
58. Buzsaki G & Draguhn A (2004) Neuronal oscillations in cortical networks. *Science* 304(5679):1926-1929.
59. Buffalo EA, Fries P, Landman R, Liang H, & Desimone R (2010) A backward progression of attentional effects in the ventral stream. *Proceedings of the National Academy of Sciences of the United States of America* 107(1):361-365.
60. Buffalo EA, Fries P, Landman R, Buschman TJ, & Desimone R (2011) Laminar differences in gamma and alpha coherence in the ventral stream. *Proceedings of the National Academy of Sciences of the United States of America* 108(27):11262-11267.
61. Chalk M*, et al.* (2010) Attention reduces stimulus-driven gamma frequency oscillations and spike field coherence in V1. *Neuron* 66(1):114-125.
62. Shin J & Talnov A (2001) A single trial analysis of hippocampal theta frequency during nonsteady wheel running in rats. *Brain research* 897(1-2):217-221.
63. Geisler C, Robbe D, Zugaro M, Sirota A, & Buzsaki G (2007) Hippocampal place cell assemblies are speed-controlled oscillators. *Proceedings of the National Academy of Sciences of the United States of America* 104(19):8149-8154.
64. Colgin LL (2013) Mechanisms and functions of theta rhythms. *Annual review of neuroscience* 36:295-312.
65. Worden MS, Foxe JJ, Wang N, & Simpson GV (2000) Anticipatory biasing of visuospatial attention indexed by retinotopically specific alpha-band electroencephalography increases over occipital cortex. *The Journal of neuroscience : the official journal of the Society for Neuroscience* 20(6):RC63.
66. Busch NA & VanRullen R (2010) Spontaneous EEG oscillations reveal periodic sampling of visual attention. *Proceedings of the National Academy of Sciences of the United States of America* 107(37):16048-16053.
67. Landau AN & Fries P (2012) Attention samples stimuli rhythmically. *Current biology : CB* 22(11):1000-1004.
68. Landau AN, Schreyer HM, van Pelt S, & Fries P (2015) Distributed Attention Is Implemented through Theta-Rhythmic Gamma Modulation. *Current biology : CB* 25(17):2332-2337.
69. Fiebelkorn IC, Saalmann YB, & Kastner S (2013) Rhythmic sampling within and between objects despite sustained attention at a cued location. *Current biology : CB* 23(24):2553-2558.
70. Holcombe AO & Chen WY (2013) Splitting attention reduces temporal resolution from 7 Hz for tracking one object to <3 Hz when tracking three. *Journal of vision* 13(1):12.

Legends

Fig. 1. Average power and phase locking spectra for the two macaques. (*A*) Average power spectrum of the ECoG LFP in V1 and V4, for monkey K, during attentional monitoring of a drifting grating. Data around the 50 Hz line-noise frequency and harmonics is not shown. (*B*) Same as *A*, but for monkey P. (*C*) Average phase locking (PPC) spectrum across all possible site pairs within and between V1 and V4, for monkey K. The shading (hardly visible behind the lines) shows the 95% confidence interval based on a bootstrap procedure across trials. (*D*), Same as *C*, but for monkey P.

Fig. 2. Average low-frequency LFP power spectra and their modulation by selective attention. (*A*) Average LFP power spectra in area V1 with attention toward (red) and away (blue) from the activating stimulus. The gray-shaded region indicates frequencies with a significant difference between attention conditions ($p<0.05$; non-parametric permutation test with correction for multiple comparisons across frequencies). (*B*) Same as *A*, but for area V4. (*C*) Same as *A*, but showing the power residuals after removing the $1/f^n$ component of the power spectrum through robust regression (see Materials and Methods). (*D*) Same as *C*, but for area V4.

Fig. 3. Average low-frequency LFP phase-locking (PPC) spectra and their modulation by selective attention. (*A*) Average LFP phase locking between sites within area V1 with attention toward (red) and away from (blue) the activating stimulus. The gray-shaded region indicates frequencies with a significant difference between attention conditions ($p<0.05$; non-parametric permutation test with correction for multiple comparisons across frequencies). (*B*) Same as *A*, but between sites within area V4. (*C*) Same as *A*, but between sites in area V1 and sites in area V4.

Fig. 4. The theta rhythm coextends with the visually induced gamma rhythm. (*A*) Visually induced LFP gamma-band power, as a function of spatial location in V1 (indicated by blue outline) and V4 (indicated by green outline). (*B*) Same as *A*, but showing LFP theta-band power after removing the $1/f^n$ component. (*C*) Correlation between 1) visually induced gamma-band power and 2) the power ($1/f^n$ removed) at the frequency indicated on the x-axis, across recording sites in area V1. Colored lines on the bottom indicate frequencies with significant correlations with attention toward (red) or away from (blue) the activating stimulus ($p<0.05$; non-parametric permutation test with correction for multiple comparisons across frequencies). The gray line on the bottom indicates frequencies with a significant difference in correlation between the attention conditions (same test). (*D*) Same as *C*, but for area V4.

Fig. 5. Average low-frequency Granger causality (GC) spectra between V1 and V4 sites. (*A*) Average GC-influence spectra between V1 and V4 in the feedforward (green) and feedback directions (black). The gray-shaded regions indicate frequencies with a significant difference between bottom-up and top-down ($p<0.05$; non-parametric permutation test with correction for multiple comparisons across frequencies). (*B*) Average GC-influence spectra between V1 and V4 in the feedforward direction, with attention toward (red) and away from (blue) the

activating stimulus. The gray-shaded regions indicate frequencies with a significant difference between attention conditions ($p<0.05$; non-parametric permutation test with correction for multiple comparisons across frequencies). Frequency regions with significant positive and negative attention effects were directly abutting to each other, and therefore the gray region is continuous. (*C*) Same as *B*, but for the feedback direction.

Fig. 6. Theta-gamma phase-amplitude coupling (PAC) in visual cortex. (*A*) LFP power of one example site in the 50-150 Hz range (y-axis) as a function of time relative to the theta trough (x-axis). (*B*) Grand-average PAC as a function of the frequency defining the power (y-axis) and the frequency defining the phase (x-axis). The semitransparent gray mask indicates frequency pairs with non-significant PAC ($p<0.05$; non-parametric permutation test with correction for multiple comparisons across frequency pairs). The black area indicates frequency pairs excluded from the analysis (see Materials and Methods).

Fig. 7. Modulation of PAC by selective attention. Average PAC in area V1 with attention toward (*A*) and away from (*B*) the activating stimulus. (*C*) Average PAC difference in area V1 between the two attention conditions shown in *A* and *B*. The semitransparent gray mask indicates frequency pairs with non-significant PAC ($p<0.05$; non-parametric permutation test with correction for multiple comparisons across frequency pairs). The black area indicates frequency pairs excluded from the analysis (see Materials and Methods). (*D*), (*E*), (*F*), Same as *A*, *B*, *C*, but for area V4.

Fig. 8. Visual theta remains after microsaccade removal. (*A*) MS-LFP PPC as a function of frequency, showing a clear theta peak. The shading shows the 95% confidence interval based on a bootstrap procedure across MSs. (*B*) V1-V1 PPC in the attend-away condition as a sensitive metric of V1 theta rhythmicity, calculated for different sets of epochs, which remove MSs with increasing stringency. Dark blue line: All available epochs (N=1917); Medium blue line: Epochs excluding MSs, that exceeded the mean eye speed by 5 SD (N=827); Light blue line: Epochs excluding MSs, that exceeded the mean eye speed by 3 SD (N=446).

Fig. 9. Attention contrast, excluding epochs with microsaccades. (*A*) Average LFP power spectra in area V1 after removing the $1/f^n$ component, with attention toward (red) and away (blue) from the activating stimulus. (*B*) Same as *A*, but for area V4. (*C*) Average LFP phase locking between sites in area V1 and sites in area V4, with attention toward (red) and away from (blue) the activating stimulus. (*D*), (*E*) Same as *C*, but for pairs of sites within area V1 (*D*) and area V4 (*E*). (*A-E*) The gray-shaded region indicates frequencies with a significant difference between attention conditions ($p<0.05$; non-parametric permutation test with correction for multiple comparisons across frequencies). (*F*), (*G*) Average PAC in area V1 with attention toward (*F*) and away from (*G*) the activating stimulus. (*H*) Average PAC difference in area V1 between the two attention conditions. (*F-H*) The semitransparent gray mask indicates frequency pairs with non-significant PAC ($p<0.05$; non-parametric permutation test with correction for multiple comparisons across frequency pairs). The black area indicates frequency pairs excluded from the analysis (see Materials and Methods).

Fig. 10. Attention contrast, controlled for microsaccade (MS) rate. Same analyses as shown in Figure 8, but after equating the MS rate. (*A*) Cumulative distribution of MS rate with attention toward (red) and away (blue) from the activating stimulus. Solid lines show data before stratification; dashed lines show data after stratification. Note that after stratification, the lines for the two attention conditions overlap essentially perfectly. (*B*) Average LFP power spectra in area V1 after removing the $1/f^n$ component, with attention toward (red) and away (blue) from the activating stimulus. (*C*) Same as *B*, but for area V4. (*D*) Average LFP phase locking between sites in area V1 and sites in area V4, with attention toward (red) and away from (blue) the activating stimulus. (*E*), (*F*) Same as *D*, but for pairs of sites within area V1 (*E*) and area V4 (*F*). (*B*-*F*) The gray-shaded region indicates frequencies with a significant difference between attention conditions ($p<0.05$; non-parametric permutation test with correction for multiple comparisons across frequencies). (*G*) Average PAC difference in area V1 between the two attention conditions. The semitransparent gray mask indicates frequency pairs with non-significant PAC ($p<0.05$; non-parametric permutation test with correction for multiple comparisons across frequency pairs). The black area indicates frequency pairs excluded from the analysis (see Materials and Methods).

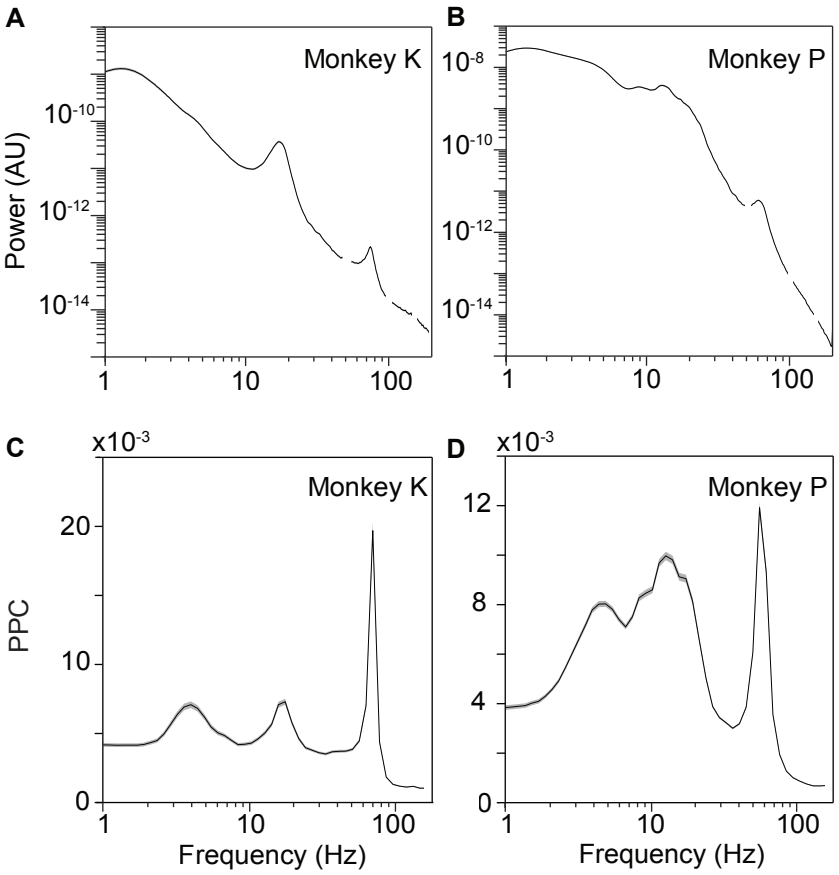

Figure 1
Spyropoulos et al.

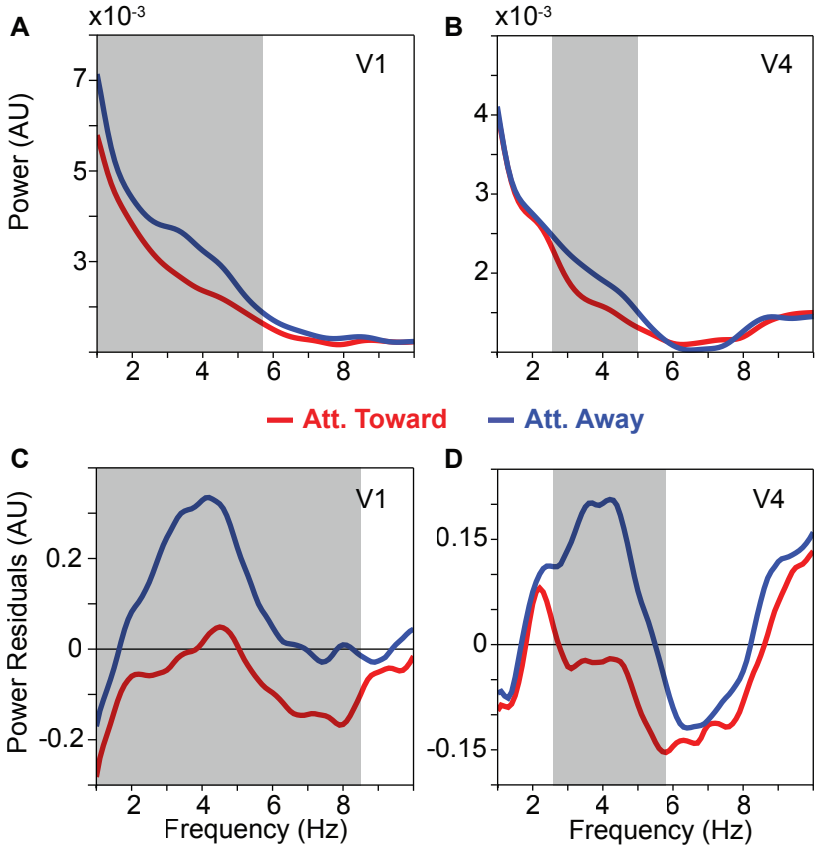

Figure 2

Spyropoulos et al.

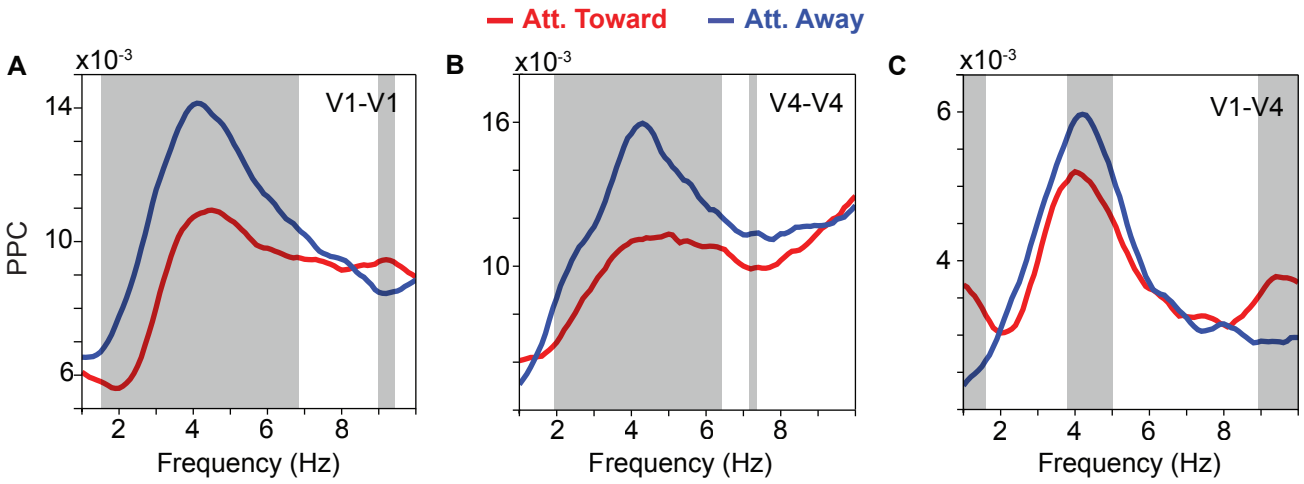

Figure 3
Spyropoulos et al.

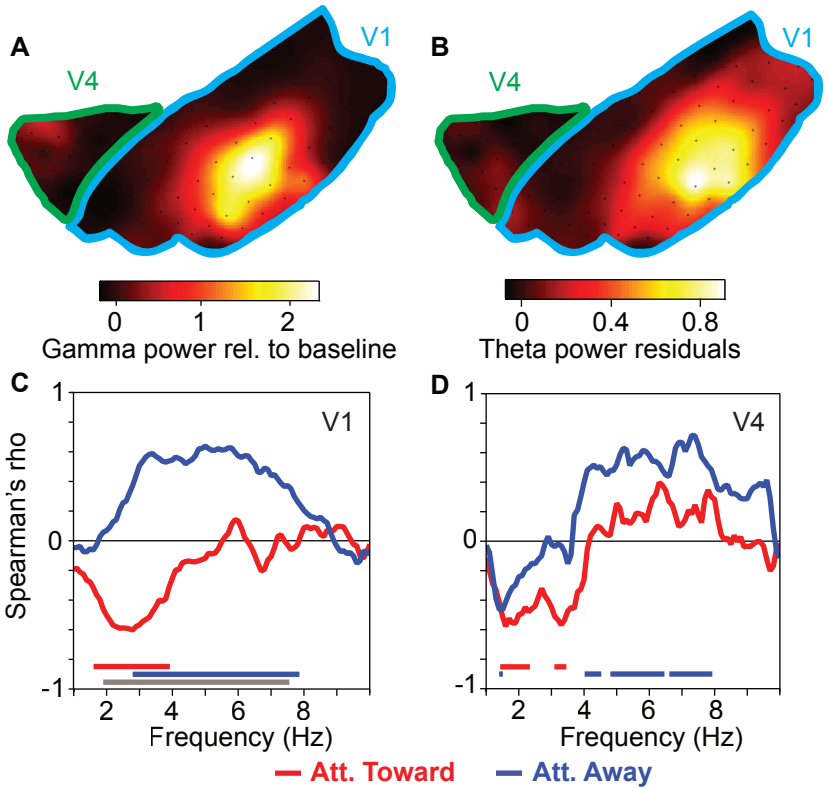

Figure 4

Spyropoulos et al.

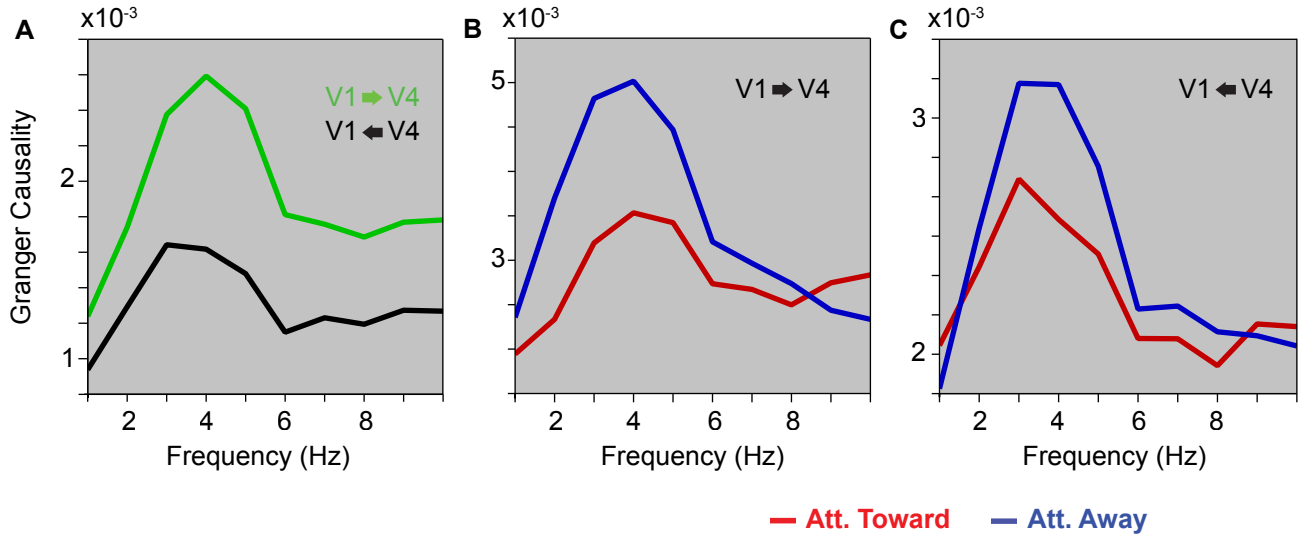

Figure 5
Spyropoulos et al.

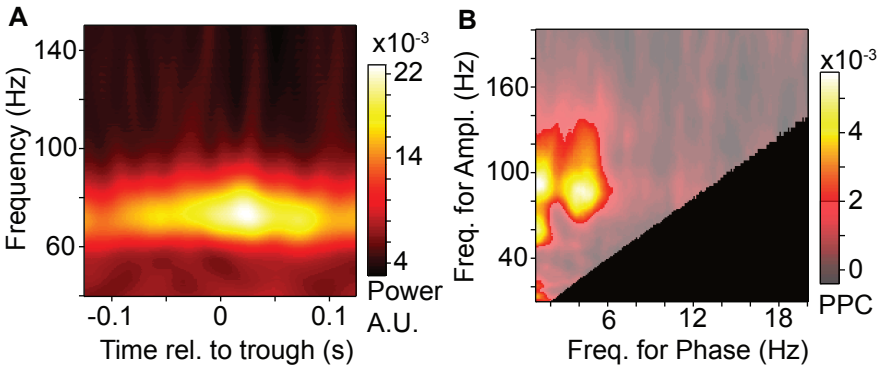

Figure 6
Spyropoulos et al.

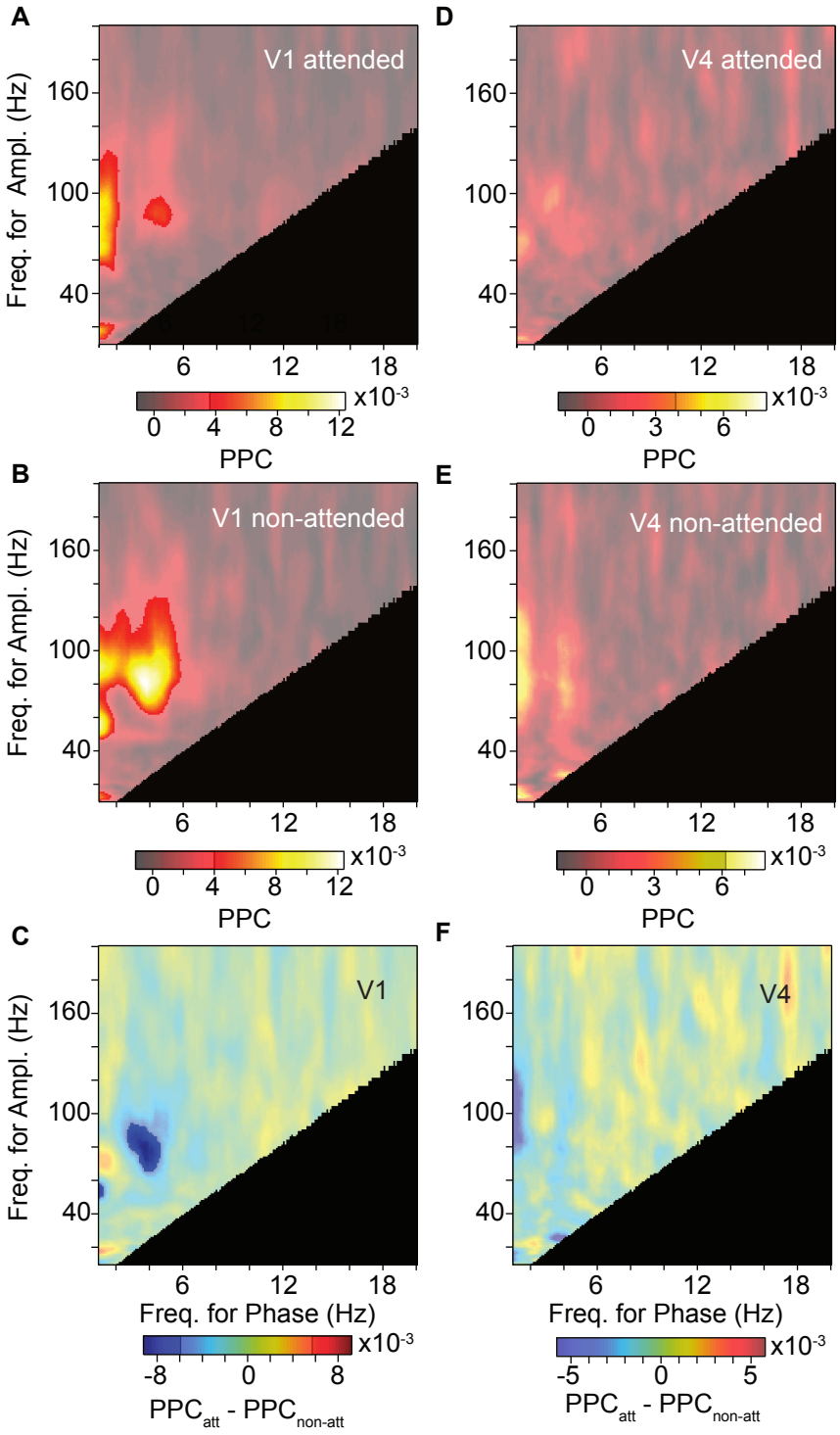

Figure 7

Spyropoulos et al.

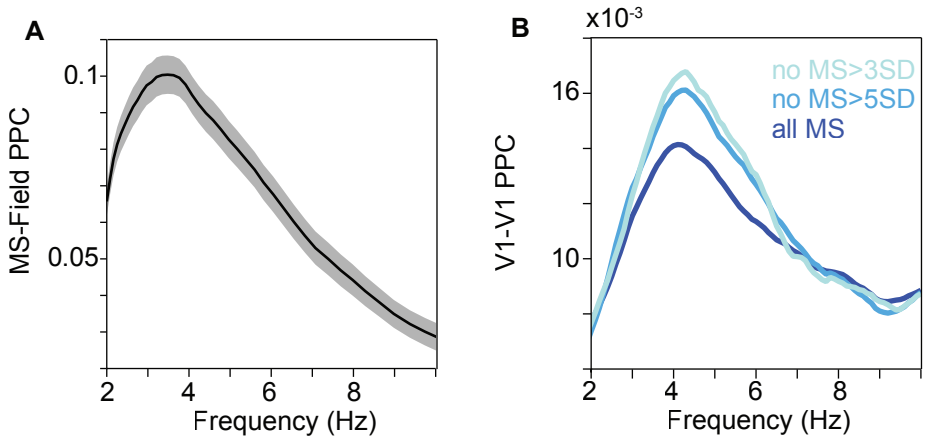

Figure 8
Spyropoulos et al.

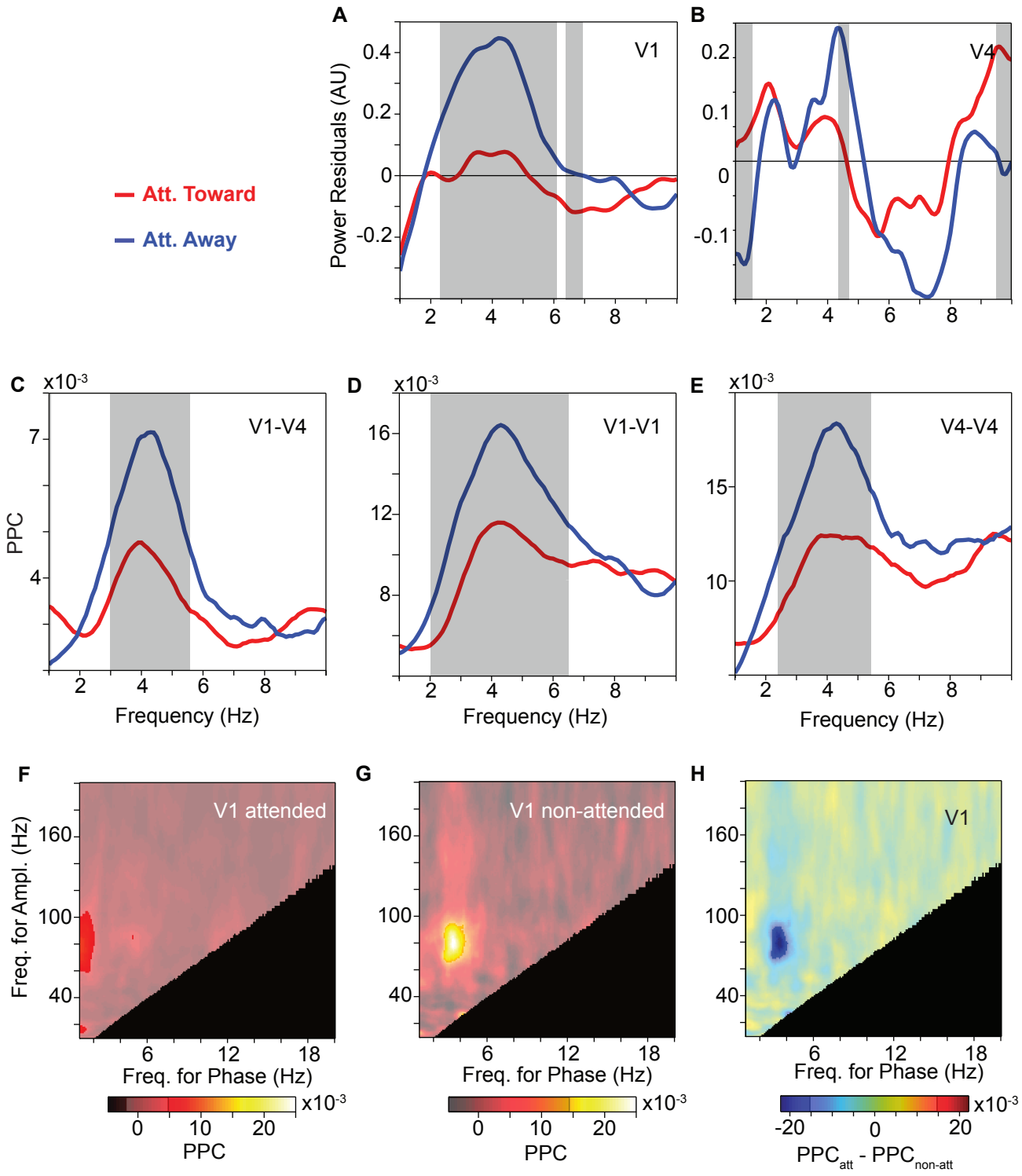

Figure 9
Spyropoulos et al.

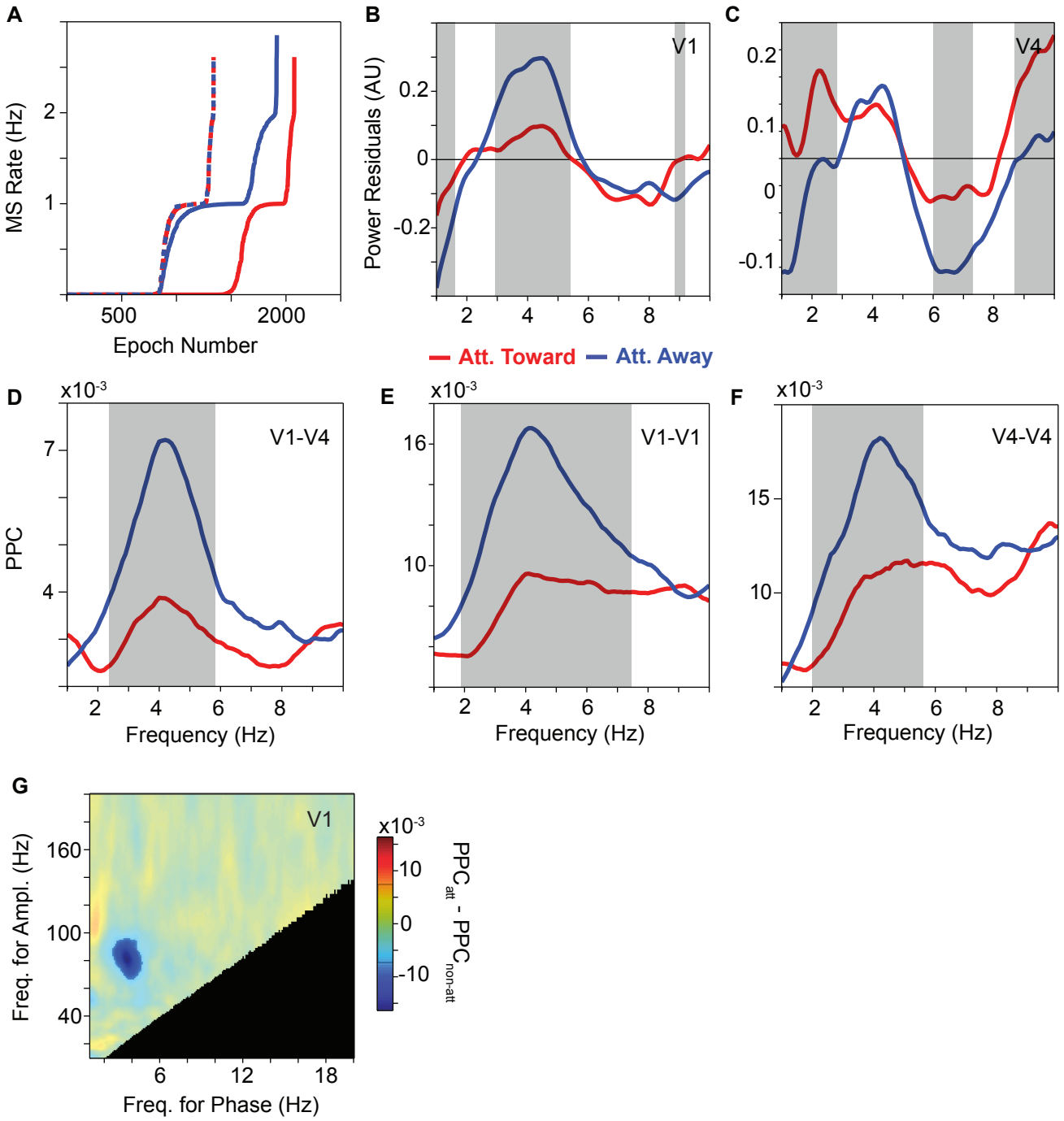

Figure 10
Spyropoulos et al.